Wave-like activity patterns in the neuropil of striatal cholinergic interneurons in freely moving mice represent their collective spiking dynamics

Rotem Rehani[1†], Yara Atamna[1†], Lior Tiroshi[1†], Wei-Hua Chiu[1], José de Jesús Aceves Buendía[1‡], Gabriela J. Martins[2], Gilad A. Jacobson[1] and Joshua A. Goldberg[1]

[1]Department of Medical Neurobiology, Institute of Medical Research Israel – Canada, The Faculty of Medicine, The Hebrew University of Jerusalem, 9112102, Jerusalem, Israel

[2]Zuckerman Mind Brain Behavior Institute, Columbia University, New York, NY, 10027, USA

[†]**Equal first author**

[‡]Current Address: Departamento de Neurología y Psiquiatría, Instituto Nacional de Ciencias Médicas y Nutrición Salvador Zubiran, México

Running Title: Spatiotemporal cholinergic activity patterns in striatum

Corresponding Author:

Joshua A. Goldberg, PhD

Department of Medical Neurobiology

Institute of Medical Research Israel-Canada

The Faculty of Medicine

The Hebrew University of Jerusalem

Ein Kerem Campus

POB 12272

9112102 Jerusalem, Israel

Phone +972-2-675-7385

Email: joshg@ekmd.huji.ac.il

Abstract

Cholinergic interneurons (ChIs) are believed to form synchronous cell assemblies that modulate striatal microcircuitry and possibly orchestrate local dopamine release. We expressed genetically encoded calcium indicators (GECIs) selectively in ChIs and visualized dorsal striatum in freely moving mice using microendoscopes. Bouts of synchronous activation of the cholinergic neuropil revealed wave-like patterns of activity that preceded the signal from individual somata. To investigate the nature of the neuropil signal and why it precedes the somatic signal, we target-patched GECI-expressing ChIs in acute striatal slices while imaging them with single- and multiphoton microscopy. We found that only back-propagating action potentials but not synchronous optogenetic activation of thalamic inputs elicits observable calcium transients in ChI dendrites. Our data suggest that the spatiotemporal neuropil patterns are a newly described physiological measure of the collective recurrent ChI network activity.

Key Words:
local field potential (LFP); GCaMP6s; spatiotemporal patterns; traveling wave; gradient refractive index (GRIN) lens; two-photon laser scanning microscopy; pacemaker; channelrhodopsin-2

Introduction

Striatal cholinergic interneurons (ChIs) are the main population of tonically active neurons (TANs) whose pause response is associated with the presentation of reward or with stimuli that are associated with reward (Anderson, 1978; Aosaki, Graybiel, & Kimura, 1994; Goldberg, 2004; Goldberg et al., 2002; Kimura, Rajkowski, & Evarts, 1984; Raz, Feingold, Zelanskaya, Vaadia, & Bergman, 1996). It was hypothesized long ago that when pausing ChIs form synchronous striatal cell assemblies (Graybiel, Aosaki, Flaherty, & Kimura, 1994). These assemblies collectively modulate neuronal excitability, synaptic transmission and synaptic plasticity in the striatal microcircuitry (Calabresi, Centonze, Gubellini, Pisani, & Bernardi, 2000; Goldberg, Ding, & Surmeier, 2012; Pakhotin & Bracci, 2007; Pisani, Bernardi, Ding, & Surmeier, 2007). This hypothesis has been buttressed by recent *ex vivo* data showing

that synchronous activation of ChIs can lead to the release of dopamine, GABA and glutamate in the striatum (Cachope et al., 2012; Chuhma, Mingote, Moore, & Rayport, 2014; English et al., 2011; Nelson et al., 2014; Threlfell et al., 2012). Multiple electrode recordings in primates have shown that TANs exhibit some degree of synchrony which increases in experimental parkinsonism (Apicella, Legallet, & Trouche, 1997; Ravel, Legallet, & Apicella, 2003; Raz et al., 1996). With the advent of genetically encoded calcium indicators (GECIs) it is now possible to visualize molecularly identified ChIs in freely moving mice (Mank & Griesbeck, 2008). The advantage of GECIs (over electrophysiological recordings, for example) is that in conjunction with advanced imaging techniques – such as head-fixed multiphoton or microendoscopy in freely moving mice – they enable longitudinal studies of the simultaneous activity of dozens of somata (Ghosh et al., 2011). This is a powerful tool for probing the collective dynamics of neuronal assemblies and to study how these assemblies change through training or other manipulations (Lin & Schnitzer, 2016).

Two aspects of GECI signals from ChIs require careful consideration which precludes simply emulating the analysis conducted on GECI signals from other neuronal types. Firstly, the majority of the studies published to date have reported the activity of neuronal populations, such as cortical or hippocampal pyramidal neurons, that – unlike ChIs – are relatively quiescent with sub-Hertz spontaneous firing rates *in vivo* until activated by synaptic input (Karnani et al., 2016; Malvache, Reichinnek, Villette, Haimerl, & Cossart, 2016; Redish et al., 2001; Rubin, Geva, Sheintuch, & Ziv, 2015). The commonly used GECIs, such as the GCaMPs, typically have a large dynamic range (>50) (Chen et al., 2013; Nakai, Ohkura, & Imoto, 2001) implying that in a quiescent neuron they should be extremely faint. In contrast, ChIs are autonomous pacemakers that discharge even in the absence of synaptic activation (Bennett, Callaway, & Wilson, 2000; Goldberg, Teagarden, Foehring, & Wilson, 2009; Surmeier, Mercer, & Chan, 2005), which means that these neurons may never be faint. Because the law of mass action dictates that the fluctuations in fluorescence be normalized by a basal level of fluorescent (denoted F_0) (Grynkiewicz, Poenie, & Tsien, 1985), it is possible that the interpretation of the fluorescent signal is flawed, because it will disregard this baseline value, even though it may represent basal discharge.

The second aspect is the issue of background signals. In most studies of other neuronal types the background activity is thought to arise from out-of-focus neurons,

hemodynamics (due to the auto-fluorescence of blood vessels) and other artifacts such as motion or photo-bleaching of dyes (Pnevmatikakis et al., 2016; Zhou et al., 2018). Thus, the working assumption is usually that the background signal is something that needs to be removed in order to extract a cleaner neuronal signal. Two approaches have been used to subtract the background signal. The first is a heuristic and involves estimating the background fluctuations in the vicinity of a given soma. This signal (or a weighted version of it) is subtracted from the somatic signal (Klaus & Plenz, 2016; Stamatakis et al., 2018; Zhou et al., 2018). The logic is simple. Due to the substantial depth-of-field of the imaging system, any signal observed in the vicinity is likely to contaminate the pixels in the soma and must therefore be subtracted. The other approach builds on the fact that the background signal tends to be highly correlated (almost uniform) in space, and therefore lends itself to being modeled as a global background signal composed of a DC term plus some low spatial frequency components. By adding this assumption to an assumption regarding the parametric exponential shape of calcium events that accompany individual spikes, this approach has yielded sophisticated algorithms which simultaneously estimate independent neuronal sources while subtracting a global model of the background (Klaus et al., 2017; Pnevmatikakis et al., 2016; Zhou et al., 2018).

It is possible that a large component of the background signals is not out-of-focus somatic signals but rather calcium influx due to propagation and/or back-propagation action potentials throughout the ChIs' axonal and dendritic arbors, respectively. Under these circumstances, these background signals should be tightly related to the network state of the ChI network, implying that the background signal could provide a physiological readout of the entire ChI network. This situation is reminiscent of the status of local field potentials (LFPs) in the extracellular electrophysiological recording. While on a practical level they are subtracted in order to better extract spiking activity, theoretical and experimental studies have revealed the mechanism of how LFPs are generated and have shown that they actually reflect a global mode of network activity (Bullock, 1997; Donoghue, Sanes, Hatsopoulos, & Gaál, 1998; Goldberg, 2004).

In the current study, we report – for the first time – the presence of traveling wave-like activity in the GECI signals from striatal cholinergic neuropil in freely moving mice imaged with microendoscopes. In order to better understand the origin of the neuropil signal

we use wide field ("one-photon") and two-photon laser scanning microscopy (2PLSM) imaging of GECI signals from ChIs in acute striatal slices. The combination of approaches leads us to the conclusion that to a large degree the spatiotemporal patterns observed in the cholinergic neuropil arise from back-propagating APs (bAPs) in the dendritic arbors. As a summation of many cholinergic processes the background activity, like LFPs, represents a readout of the collective discharge of ChIs.

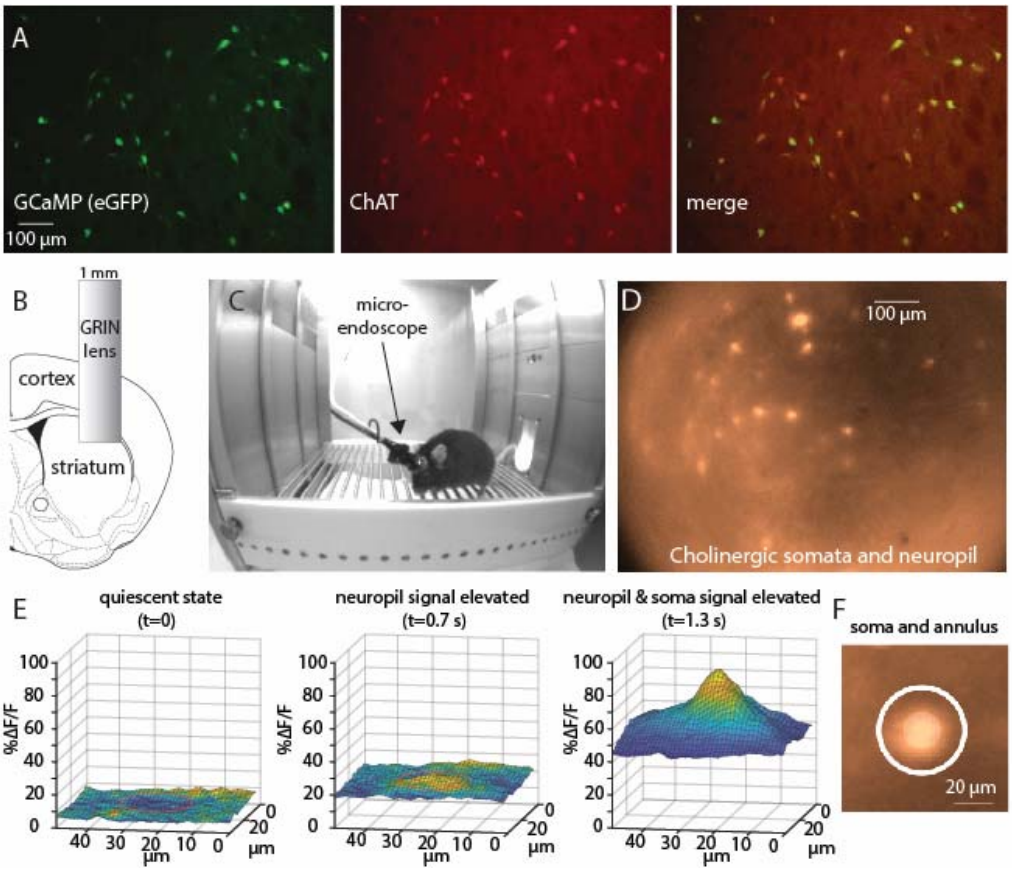

Figure 1. Imaging of the striatal cholinergic network in freely moving mice reveals both somatic and neuropil signals. A. Immunohistochemical analysis of dorsal striatum of choline acetyltransferase (ChAT)-cre mice stereotactically injected with adeno-associated viruses harboring floxxed GCaMP6s demonstrates its selective expression in ChIs. B. A 1 mm diameter GRIN lens is implanted into dorsolateral striatum following aspiration of cortical tissue. C. Implanted mouse with a microendoscope mounted on its head moves freely in a behavior chamber. D. Image via lens in freely moving mouse reveals a GCaMP6s signal from 39 identifiable somata and from the surrounding neuropil. E. 3-D rendition of a patch of the *ΔF/F* signal surrounding a soma reveals that an elevation in the neuropil signal precedes elevation of the somatic signal (region of soma indicated by a red circle). F. Illustration of the sampling of a somatic region-of-interest (central circle) and a surrounding (white) annular region.

Results

Synchronous spatiotemporal wave-like patterns in striatal cholinergic neuropil of freely moving mice

The dorsolateral striatum (DLS) of choline acetyltransferase (ChAT)-cre mice was transfected with adeno-associated viruses (AAVs) harboring cre-dependent CGaMP6s, causing this genetically encoded calcium indicator (GECI) to express selectively in ChIs (Fig. 1A). Following implantation of GRIN lens in the transfected area (Fig. 1B), imaging an area of approximately 600 μm by 900 μm through the lens using a miniaturized endoscope in freely-moving mice (Fig. 1C) revealed spatiotemporal fluctuations in fluorescence in the cholinergic neuropil. These fluctuations were characterized by recurring, rapid bursts of activation that permeated the entire field-of-view (FoV) and that slowly decayed (Supplementary Movie 1). Embedded within the neuropil were several dozen somata of individual ChIs that also exhibited substantial fluctuations in fluorescence (Fig. 1D). Due to the depth-of-field of the 0.5 numerical aperture (NA) GRIN lens, the pixels from somata also contain contributions of fluorescence from the dense, space-filling cholinergic axonal and dendritic processes (Chang, Wilson, & Kitai, 1982; Difiglia, 1987; Kawaguchi, 1992; Wilson, Chang, & Kitai, 1990) traversing above and below the somata and possibly from other out-of-focus fluorescent somata. One expression of this is that the somatic fluctuations are always superimposed upon the temporal fluctuations of the surrounding pixels that contain the same contribution from the by-passing neuropil (Fig. 1E, Supplementary Movie 2).

To estimate the spatiotemporal structure of the neuropil signal and to compare it to the somatic activity we analyzed activity in annuli surrounding each of the somata in the FoV (Fig. 1F). In Fig. 2A we depict a color-coded matrix of the fluctuations in fluorescence *($\Delta F/F$)* as a function of time with each row representing an individual annulus. This matrix reveals that the neuropil is composed of dramatic increases in $\Delta F/F$ that are highly synchronous across the entire FoV (as is evident from the near-identical signal in the various rows of the matrix), and that decay slowly, as can be seen in the population average of all the annuli (Fig. 2B). In comparison, individual somata exhibited more distinct dynamics, once the signal from each annulus was subtracted from its corresponding soma (Fig. 2C).

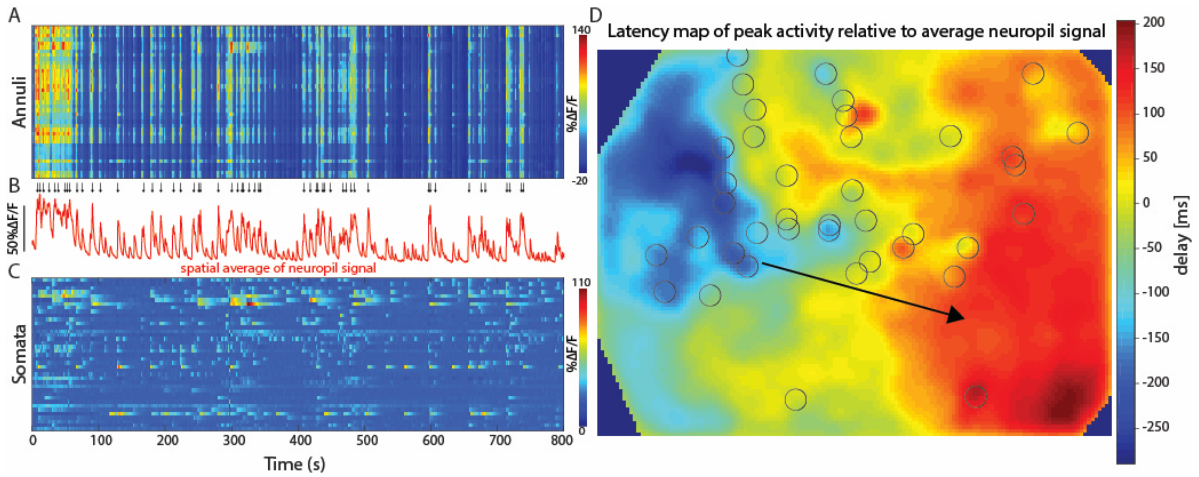

Figure 2. Spatiotemporal wave-like propagation of neuropil signal in dorsolateral striatum in freely moving mouse. A. Color coded matrix of activity of neuropil $\Delta F/F$ signal sampled from the annuli surrounding 39 somata scattered in the field-of-view. Time is represented along the horizontal axis. Each row corresponds to an individual annulus. B. population average of signals from all annuli. Arrows above represent peaks of strong network activation (see Materials and Methods). C. Color coded activity of the 39 somata $\Delta F/F$ signals, after subtraction of the surrounding annular signal. D. map of time delays of the neuropil signal peaks (in each pixel) relative to the time of peak of the average annular signal (map filtered with a 2D Gaussian filter). The arrow represents the extracted best fit direction of the velocity vector of propagation. Circles indicate the location of the annuli surrounding the individual somata.

Close examination of the recurring bursts of activity (Supplementary Movie 1) suggested that the neuropil signal in this mouse propagates in the plane of the image from top left to bottom right. To test this, we identified peaks of large calcium fluctuations in the average annular $\Delta F/F$ signal (see arrows in Fig. 2B). To visualize the propagation, we calculated for every pixel in the image the average latency with which its $\Delta F/F$ signal peaked relative to the timing of the peak of the population average. A smoothened version of this map (Fig. 2D) demonstrates that there is an orderly advancement of peak times from top left to bottom right. To estimate the velocity vector of this propagation, we calculated the least-square linear fit to this latency map, from which a velocity vector describing the overall average propagation can be calculated (see Materials and Methods), and whose direction is depicted as an arrow along the latency map (Fig. 2D). An example of the same analysis from another mouse is provided in the supplementary material (Supplementary Movie 3). Thus, we conclude that the cholinergic neuropil signal propagates through the striatum creating a visible wave-like progression along the dorsal surface of the striatum.

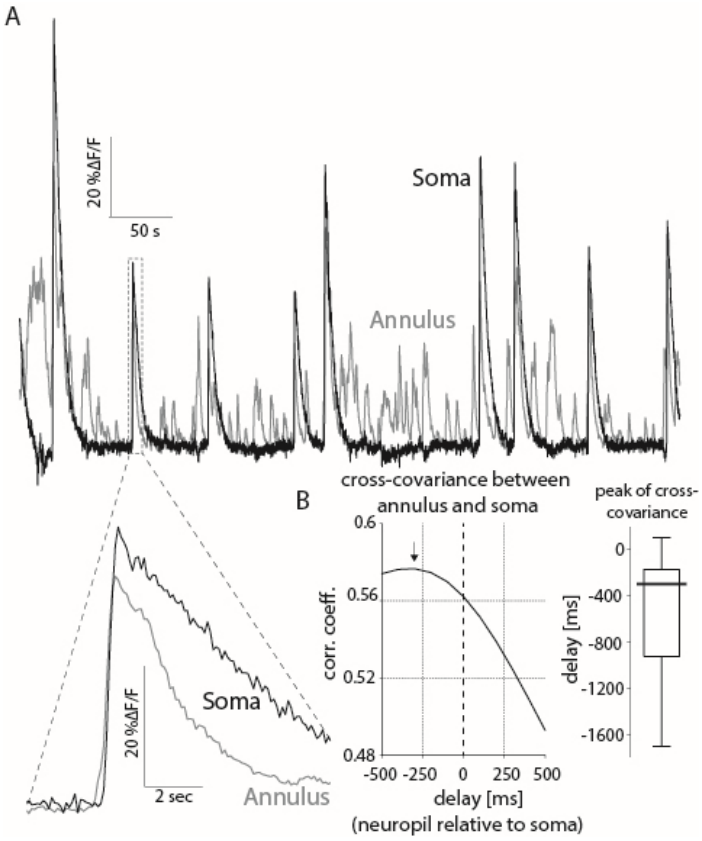

Figure 3. Annular (neuropil) signal precedes somatic signal in freely moving mice. A. Calcium (*ΔF/F*) signal from a soma-annulus pair (one event is magnified in bottom left). B. Left: cross-covariance function between the somatic and annular signals (depicted in panel A), calculated over 20 minutes. Location of peak is marked by an arrow. Right: Boxplot of peak delays from the soma-annulus pairs.

The neuropil calcium signal precedes the somatic signal

As seen above (Fig. 1E, Supplementary Movie 2), comparison of the activity of a given soma (after subtraction) and its surrounding neuropil signal (taken from the corresponding annulus) suggests that even though the activity of the ROI and annulus are quite distinct, every time a soma is activated, this activation is preceded slightly by an activation of the surrounding neuropil signal (Fig. 3A). To quantify this effect, we calculated the cross-covariance function (CCF) between fluorescence signals from individual somata and their corresponding annuli (Fig. 3B). Given that the cholinergic neuropil is almost entirely intrinsic to the striatum (Contant, Umbriaco, Garcia, Watkins, & Descarries, 1996; Dautan et al., 2014; Mesulam, Mash, Hersh, Bothwell, & Geula, 1992), the neuropil signal would be expected to peak at the same time as the somatic signals would. However, our analysis suggests that the neuropil (annuli) signal preceded the somata signal by approximately 300 ms (Fig. 3B). A possible explanation for this result is that the neuropil signal precedes the somatic signals because the former represents input to the latter. It is possible that activation

of synaptic inputs generates elevations in dendritic calcium levels that would manifest themselves as neuropil signals that precede the somatic discharge. Alternatively, perhaps the afferent cholinergic projection from the pedunculopontine nucleus to DLS (Dautan et al., 2014) was infected retrogradely by the striatal AAV injection and contributes to the fluorescence, thereby contributing to a fluorescent neuropil signal that precedes the somatic signal. However, these possibilities seem unlikely because 300 ms is too long a latency to be accounted for simply by synaptic delays.

Several properties of the neuropil and somatic signals are therefore still in need of elucidation. How are fluctuations in somatic fluorescence signals related to the actual discharge of cholinergic interneurons? What is the physiological process that generates the neuropil signal? What is the origin of the 300 ms delay between the peak of the neuropil and somatic signals? These questions and the curious observation of spatiotemporal wave-like patterns in the neuropil prompted us to delve deeper into the origin of the somatic and neuropil signals generated during the collective activity of ChIs.

Because ChIs are autonomously active neurons (Bennett et al., 2000; Goldberg et al., 2009; Surmeier et al., 2005), we reasoned that some degree of collective cholinergic activity would be preserved in acute striatal slices, and that we could image this activity in the ChAT-cre mice expressing GCaMP6s selectively in ChIs. We also reasoned that using two-photon laser scanning microscopy (2PLSM) would help us discriminate between somatic and neuropil signals. Due to the miniscule depth-of-field (<2 μm FWHH) of 2PLSM, the contamination of somatic imaging by out-of-focus neuropil would be negligible. Additionally, 2PLSM allows imaging of individual dendrites which are presumably a major contributor to the neuropil signal, and study precisely under what circumstances they give rise to GCaMP6s signals. By combining targeted patch clamp recordings with 2PLSM imaging we could address mechanistic questions regarding the relationship of the somatodendritic calcium signal and the electrophysiological activity of the ChIs.

Somatic GCaMP6s signals exhibit diverse temporal patterns of activity *ex vivo*

2PLSM imaging of acute striatal slices demonstrated that neuropil expressing fluorescent GCaMP6s could be observed. Moreover, the neuropil can be resolved as dendritic (and perhaps axonal) processes. The striations were devoid of GCaMP6s, in line with their

known composition of non-cholinergic afferent fibers (Wilson, 2004). Embedded within the fluorescent neuropil processes several (up to 10 per experiment) ChI somata could be visualized. In the example depicted in Fig. 4A, we were able to manually mark 9 distinct somata for imaging and extract traces of *ΔF/F* that exhibited autonomous calcium fluctuations in the transfected neurons (Fig. 4B). In some traces, calcium transients that appear to correspond to individual action potentials could be observed (top 3 traces). Collectively, these traces demonstrated that the temporal structure of the fluctuations varied considerably among the somata (Fig. 4B), with some cells exhibiting large fluctuations in *ΔF/F* while others exhibited relatively uneventful traces (bottom 5 traces). Interestingly, the nature of the calcium signal in individual neurons could vary considerably with time. For example, one ChI (marked by the pink arrow in Fig. 4C) exhibited large calcium fluctuations in the initial trace (Fig. 4D, upper pink trace). A few minutes later, these fluctuations died down (middle pink trace). Finally, after a few more minutes elapsed, large fluctuations resumed (bottom pink trace). Such findings are consistent with previous studies that showed that individual ChIs in acute slices can change their firing pattern from regular to irregular to bursting discharge (Bennett & Wilson, 1999; Goldberg & Wilson, 2010).

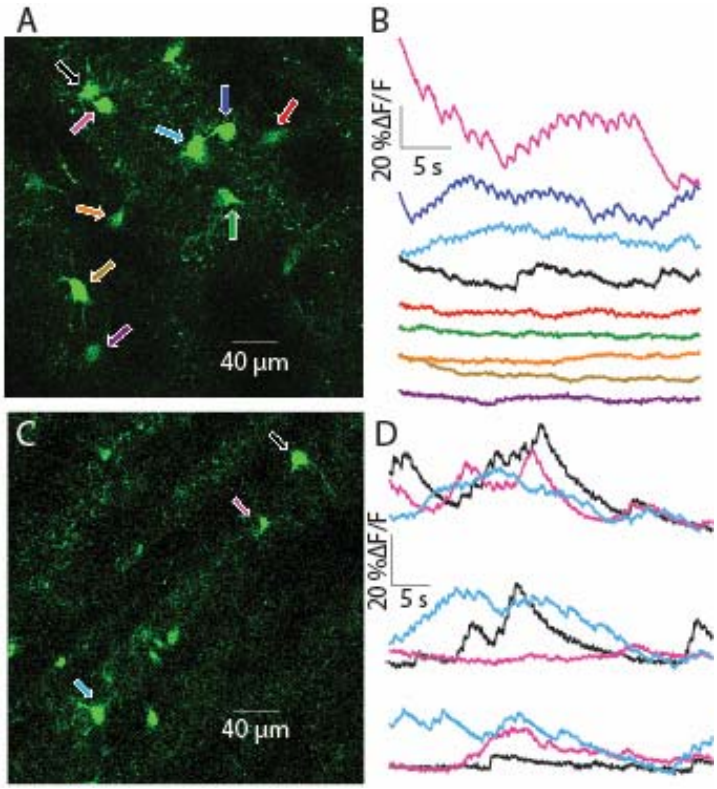

Figure 4. 2PLSM imaging of ChI somata in acute striatal slices. A. 2PLSM image of ChIs expressing GCaMP6s in an acute striatal slice. Nine individual ChIs are identified and color coded with arrows. B. Color coded traces of calcium (*ΔF/F*) signals from the 9 cells depicted in panel A. C. 2PLSM image from another mouse, with three identified and color-coded ChIs. D. Three repetitions of calcium imaging of the 3 ChIs depicted in panel C – a few minutes apart.

It is easy to make a convincing case that the GCaMP6s signal represents autonomous discharge when transients associated with individual spikes or large fluctuations in $\Delta F/F$ are observed. However, what can be said for the cells that exhibit a relatively flat and unchanging profile of fluorescence?

Limitations in interpreting somatic GCaMP6s signal from autonomously firing ChIs

As discussed in the Introduction, autonomous activity of ChIs in acute striatal slices may manifest itself as flat, unchanging fluorescence. To address this possibility, we used targeted-patch of ChIs in order to characterize the firing patterns underlying the calcium transients (Fig. 5A). We then aligned the trace from the somatic region of a cell with its corresponding electrophysiological recording. When a ChI discharged spontaneously in a bursty fashion (Fig. 5B, blue), calcium transients similar to those observed without a patch electrode (Fig. 4) were visible, and it was possible to clearly associate the electrophysiological recordings and the large calcium transients. Proximal dendrites exhibited an even clearer relationship to spiking (Fig. 5B, pink), due to the larger surface-to-volume ratio (see below). In ChIs that fired regularly (Fig. 5C), fluorescence transients associated with single actions potentials could still be identified, as long as the firing rate was sufficiently low (Fig. 5D, top). In this case, estimation of the spike triggered average (STA) of the calcium signal revealed a large $\Delta F/F$ waveform that rose after the action potential occurred and slowly decayed (Fig. 5E, top). When the same ChI discharged faster, it was no longer possible to unequivocally discern individual transients (Fig. 5D, bottom). Nevertheless, the STA revealed a $\Delta F/F$ waveform that is time-locked to the action potential (Fig. 5E, bottom), albeit a significantly smaller one than that observed during slower discharge (Fig. 5E, top). This finding suggested the tetanic-like fusing of the individual calcium transients is responsible for the decrease of the STA amplitude. If tetanic fusion of the $\Delta F/F$ signal occurs at firing rates as low as 2-2.5 spikes/s, this effect places strong constraints on the ability to read out the discharge patterns underlying the calcium transients when using GCaMP6s.

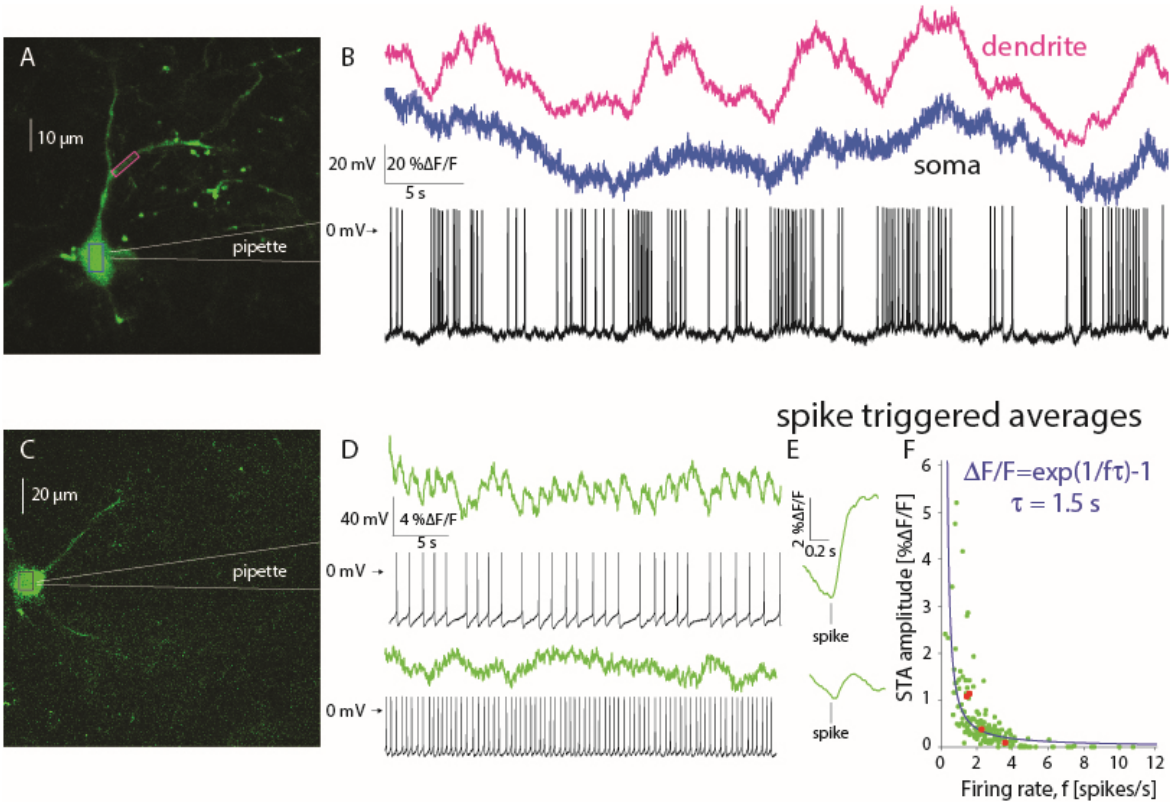

Figure 5. Estimation of autonomous discharge of ChIs using 2PLSM GCaMP6 imaging is limited to bursting or to slow regular firing neurons. A. 2PLSM imaging of somatic and dendritic calcium (*ΔF/F*) signals in conjunction with electrophysiological recording from GCaMP6s-expressing ChI. B. Somatic (blue) and dendritic (pink) *ΔF/F* signals and membrane potential of ChI depicted in panel A. C. 2PLSM somatic imaging and electrophysiological recording from another ChI. D. Somatic imaging and corresponding electrophysiological recording from ChI firing autonomously at a lower rate (top) or driven to fire faster at a higher rate (bottom). E. spike-triggered average (STA) of somatic *ΔF/F* signal (from panel D) for slow (top) and fast (bottom) discharge. F. Amplitude of STA vs. the firing rate of regularly firing ChIs. Solid blue line: fit of phenomenological model (see text).

To quantify this effect, we characterized the relationship between firing rate of the ChIs and the amplitude of the STA of the *ΔF/F* trace associated with that firing rate. Figure 5F depicts a scatter plot of the STA amplitude as a function of firing rate for *n=25* non-bursting ChIs (from *N=15* mice), where each ChI is represented by at least three points corresponding to different firing rates (e.g., red dots represent 4 measurements from the same ChI). The resulting plot (Fig. 5F) shows that the STA calcium transient amplitudes decrease as the firing rate increases. When the firing rate is too high it becomes impossible to detect the underlying spike times from the fluorescence trace alone, because the average

transient is too small to discern against a noisy background. An example for such a case is shown in Fig. 5D, bottom, where the neuron fires at ~2-2.5 Hz. Individual action potentials can no longer be discerned from the imaging trace alone even though the estimation of the STA reveals a visible waveform.

The dependence of the size of the STA on the firing rate can be captured by a simple phenomenological model (see Materials and Methods) wherein the observed calcium dynamics are simply a sum of the calcium fluorescence transients elicited by the individual action potentials. If we further assume for simplicity that the transient is exponentially shaped (with a decay time constant τ) and that the firing is perfectly periodic, we can derive an expression for the amplitude of the STA as a function of the firing rate that depends on the single parameter τ. The value of τ for the fit (blue line in Fig. 5F) is 1.5 seconds. The main determinant of this decay is the decay kinetics of GCaMP6s which is on the order of one second (Chen et al., 2013). Additionally, imaging large compartments such as somata further slows the decay kinetics (Goldberg et al., 2009).

Capacity to detect individual spikes using wide field calcium imaging is diminished

From the empirical results and the phenomenological model, it is evident that the faster the neurons fire, the smaller the size of the STA waveform. In other words, the slower the decay kinetics of the indicator the harder it is to discern individual action potentials in the calcium signals. These data demonstrate that the use of GCaMP6s, constrains the ability to detect individual calcium transients if the neuron fires faster than 2-3 spikes/s. But what resolving power is GCaMP6s expected to have under the single-photon conditions employed in the endoscopic imaging? Unlike the sensitivity of 2PLSM imaging, the endoscopic data collected from the awake behaving mouse did not seem to exhibit calcium transients corresponding to individual action potentials. One possibility is that the much slower sampling rate of the endoscope – which smears STAs (Teagarden, Atherton, Bevan, & Wilson, 2008) – and its low NA (0.5) GRIN lens objective further diminish the ability to discern individual action potentials. To test this possibility, under more controlled conditions in conjunction with electrophysiological recordings, we conducted wide-field calcium imaging of ChIs expressing GCaMP6s in acute slices under conditions that recreate the endoscope's specification, by using an EM-CCD at a sampling rate of 5-10 Hz via a 20X/0.5 NA objective.

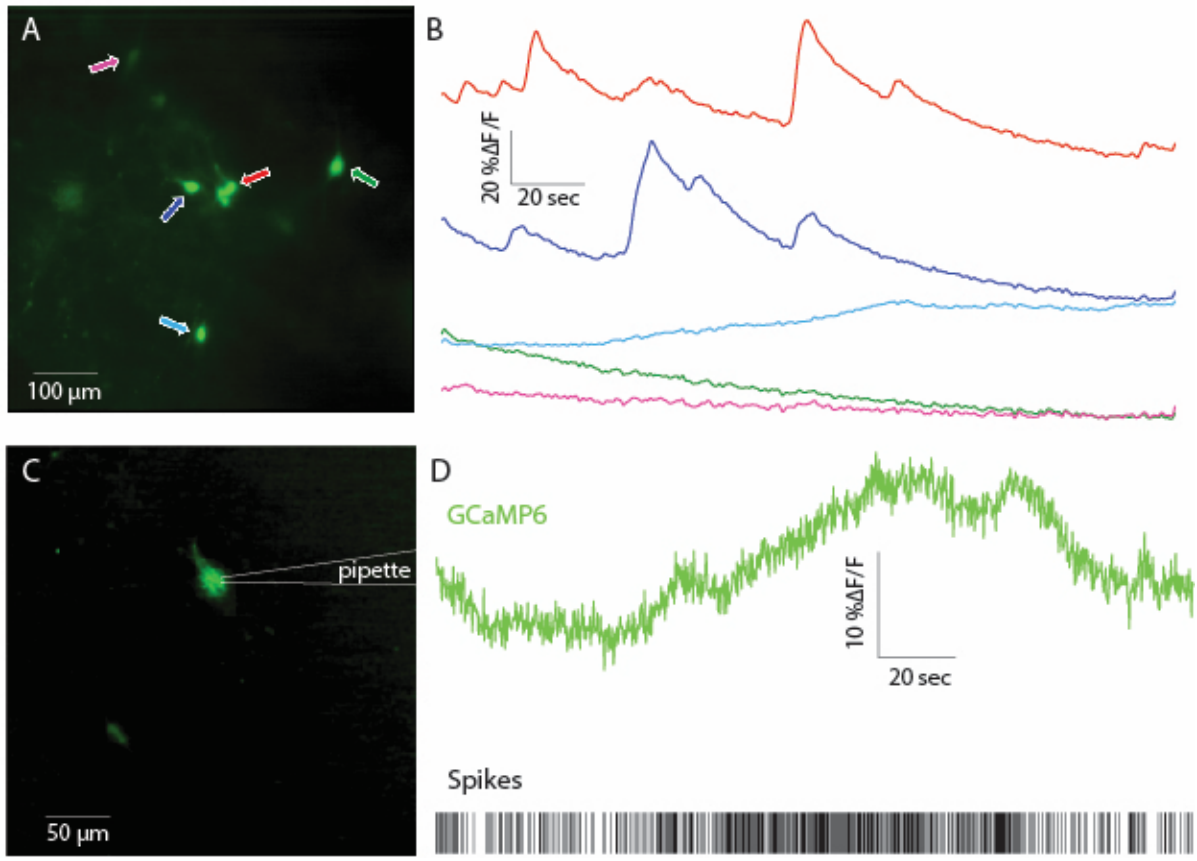

Figure 6. Wide-field one-photon imaging of ChI somata in acute striatal slices. A. Wide-field image of ChIs expressing GCaMP6s in an acute striatal slice. Five individual ChIs are identified and color coded with arrows. B. Calcium (*ΔF/F*) signal from the 5 cells depicted in panel A. C. Wide-field image from another cell recorded in cell attached mode. D. Calcium (*ΔF/F*) in conjunction with spike raster of the ChI depicted in panel C.

The wide-field imaging revealed a diffuse neuropil signal, similar to that seen *in vivo* (Fig. 6A). As with the 2PLSM imaging experiments, we were able to discern multiple ChIs per slice (Fig. 6A), and the calcium transients associated with individual neurons were variable, with some exhibiting large and slow fluctuations while others exhibiting flat traces (Fig. 6B). When we combined electrophysiological recordings with the imaging, it was possible to observe gross changes in firing rate in the *ΔF/F* signal (Fig. 6C). However, when we focused on examples where the discharge was relatively regular, it was impossible to observe fluorescence transients associated with individual spikes. Furthermore, the STAs in these cases were indistinguishable from a flat line (*n=9* neurons from *N=8* mice, data not shown).

Our conclusion is that a sufficiently slow firing rate is required in order to discern calcium transients from individual spikes, and that – in our hands – this is achieved reliably only using 2PLSM. Wide field imaging with a slow camera and a low NA objective will generate GCaMP6s signals, that follow changes in firing rate, but from which individual spikes are not detectable. Moreover, when observing a calcium trace with only small fluctuations it is difficult to determine (even with concurrent electrophysiological recordings) whether the cell is firing fast or not firing at all. The conclusion is that with the use of endoscopes one can only observe substantial fluctuations in firing rate. Moreover, because constant fluorescent signals are usually included in the baseline value (F_0), any relatively regular activity of ChIs will generate a basal fluorescence that will be removed when calculating the $\Delta F/F$ signal, and will therefore remain undetected.

Origin of the neuropil signal

The previous analysis suggests that the fluctuating somatic GCaMP6s signals observed via the endoscope extract only robust changes in the firing rate of ChIs. We next turn to consider what neural activity gives rise to the cholinergic neuropil signal observed in endoscopy. Here again we employ 2PLSM in acute striatal slices with GCaMP6s-expressing ChIs. As mentioned above, distinct dendritic processes are observed with 2PLSM throughout the transfected regions in the striatal slice. As these processes are ubiquitous, and no other cell types express the GECI, we hypothesized that ChI dendrites contribute to the blurred neuropil signal visualized with the endoscopes and the wide field calcium imaging (Fig. 1D, supplementary movies 1 & 2) (Goldberg et al., 2009).

Because of the large, global fluctuations of the neuropil signal in the endoscopic imaging, we set out to determine their source. Previous studies of calcium signals in ChIs from acute rodent slices using inorganic membrane impermeable dyes (Bennett et al., 2000; Goldberg et al., 2009; Tanimura, Lim, Aceves Buendia, Goldberg, & Surmeier, 2016) demonstrated that bAPs and even long back-propagating subthreshold depolarizations (bSDs), can open dendritic voltage-activated calcium channels (Chen et al., 2013), and generate visible dendritic calcium changes. These are certainly candidate mechanisms to generate dendritic GCaMP6s signals. However, because the neuropil signal preceded the somatic signals in the endoscopic data, we considered another possibility, that activation of

afferent glutamatergic inputs could introduce sufficient calcium influx via NMDA and calcium permeable AMPA receptors, both of which are expressed in ChIs (Aceves Buendia, Tiroshi, Chiu, & Goldberg, 2017), to generate a visible calcium signal. In order to determine which of these three scenarios – namely bAPs, bSDs or activation of ionotropic glutatmate receptors – is responsible for the dendritic signals, we compared the size of the GCaMP6s $\Delta F/F$ signals generated by each of these physiological processes.

Back-propagating action potentials are the main contributor to the neuropil signal

To determine whether bAPs or bSDs are the main contributors to the dendritic calcium signal, we target-patched ChIs, silenced them with a hyperpolarizing holding current, and injected sub- or supra-threshold depolarization currents while measuring the resulting calcium transient at a proximal dendrite. Comparison of the size of the transients evoked by back-propagating sub- and supra-threshold depolarization revealed that bAPs generated a significantly larger calcium signal in dendrites, that were quantified by the integrated fluorescence beneath the $\Delta F/F$ curve for a period of 800 ms (median bAP integrated fluorescence: 0.6875, median bSD integrated fluorescence: 0.048, $P = 7.8\times10^{-3}$, Wilcoxon signed-rank test, data not shown). This result suggests that of the first two possibilities, bAPs are the main source of the GCaMP6s neuropil signal, whereas the contribution of sub-threshold calcium entry is negligible.

In order to test whether synchronous activation of glutamatergic inputs could also generate visible calcium transients in ChI dendrites, we injected mice with AAVs harboring channelrhodopsin-2 (ChR2) with a ubiquitous promoter into the thalamic parafascicular nucleus (PfN), which gives rise to the dominant glutamatergic input to ChIs (Aceves Buendia et al., 2017; Ding, Guzman, Peterson, Goldberg, & Surmeier, 2010; Lapper & Bolam, 1992; Threlfell et al., 2012). Thus, in acute slices from these animals, ChIs expressed GCaMP6s while thalamic fibers expressed ChR2. Two-to-three weeks after transfection, we target-patched ChIs (Fig. 7A) and evoked excitatory synaptic potentials (EPSPs) in the patched ChI using full-field 470 nm LED illumination (Fig. 7B). We compared the integrated dendritic calcium signal in response to sub-threshold EPSPs to the dendritic calcium signal generated by spontaneously occurring bAPs in the same cells. The calcium transient generated by spontaneous bAPs was significantly larger than the transient that corresponded to the sub-

threshold EPSPs (Fig. 7C, median bAP transient integrated fluorescence: 0.2803, median EPSP transient integrated fluorescence: 0.0382, P = 0.0195, Wilcoxon signed-rank test. The values for subthreshold current pulses are shown, as well, for comparison).

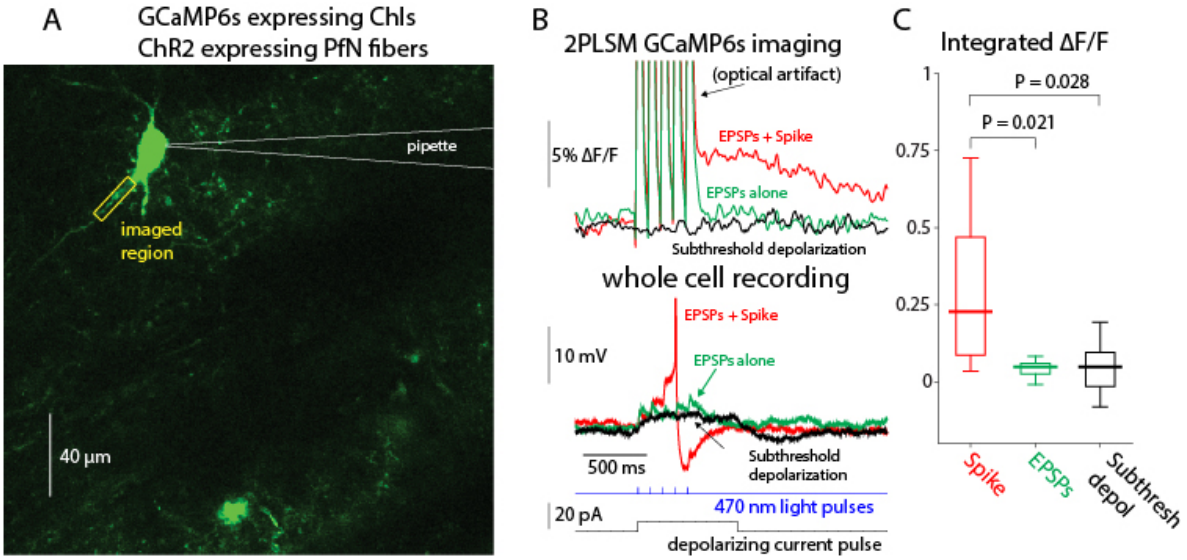

Figure 7. Dendritic GCaMP6 signals detectable using 2PLSM imaging are limited to back propagating action potentials (bAPs). A. 2PLSM imaging of somatic and dendritic calcium ($\Delta F/F$) signals in conjunction with electrophysiological recording from GCaMP6s-expressing ChI surrounded by parafascicular nucleus (PfN) fibers expressing ChR2 (not shown). B. Calcium ($\Delta F/F$) signals in response to optogenetic activation of PfN synapses elicits either a subthreshold (green) or suprathreshold (red) synaptic response (bottom) in ChI depicted in panel A. Only the spiking response elicits a detectable $\Delta F/F$ signal. Subthreshold depolarization (in another cell) does not elicit a detectable response (compare to Goldberg et al. 2009). C. Distribution of integrated $\Delta F/F$ response in response to spontaneous bAPs, subthreshold EPSPs and subthreshold depolarization.

Because the slice is filled with many fluorescent processes it was only possible to reliably identify the proximal dendrites belonging to the patch-clamped ChI. Thus, strictly speaking the previous analysis relates to calcium transients in proximal dendrites. Nevertheless, it was occasionally possible to observe bAPs infiltrating distal regions, up to 150 µm from the soma (Supplementary Fig. 1), as reported previously (Tanimura et al., 2016). We conclude that only bAPs generate a visible dendritic calcium signal. Indeed, as expected from surface-to-volume ratio considerations, and as has been shown previously with inorganic calcium indicators (Goldberg et al., 2009) the ongoing GCaMP6s $\Delta F/F$ fluctuations are significantly larger in the dendrites than in the soma (Fig. 6A & Supplementary Fig. 2), as observed by comparing STAs of dendritic transients to STAs of

somatic transients (*n=23* cells from *N=13* mice, $P = 7.35\times10^{-4}$, two-tailed Wilcoxon signed-rank test).

The neuropil signal represents a mean-field readout of the entire ChI network

In light of the above experiments, it is likely that the background activity seen in the endoscopic *in vivo* imaging results from bAPs arising from ChIs scattered throughout the striatum whose somata may not be visible but whose dendrites are within the FoV. Whenever a GCaMP-expressing ChI fires, its entire dendritic (and possibly axonal) arbor lights up. Because the dendritic arbors of ChIs overlap and cover the whole striatum (Chang et al., 1982; Difiglia, 1987; Kawaguchi, 1992; Wilson et al., 1990), a pixel whose depth of field is tens of microns integrates the fluorescent signals of bAPs from dendrites of many neurons. Nearby pixels will integrate similar signals and will therefore be highly correlated. Because this correlated signal is the sum of the activity of many cells it represents a "global mode" of ChIs activity. Because the global mode arises from the bAPs in ChIs, it can be considered a read-out of the "mean-field" of the recurrent network activity of the entire ChIs population.

If the neuropil signal is a mean-field readout of the recurrent ChI network, it would be expected that on average the peak of the somatic signals will coincide with the peak of the neuropil signal. What then gives rise to the 300 ms latency from the peak of the population response to the peak of the response of individual ChI soma? The most likely explanation is that the population (neuropil) signal represents the gradual recruitment of many ChIs. Consequently, it is slower to rise than the signal from each individual neuron (as seen in the somatic signals). A simple mathematical analogy (Supplementary Fig. 3) demonstrates that when calculating the CCF of two signals whose peaks coincide in time but where one rises more gradually to the peak than the other, then the CCF will display a peak with a negative latency, just as observed empirically (Fig. 3B). Additionally, when sampling a single neuron from a large population that is being recruited, it is expected that the onset of the signal from the single neurons will follow the population average. This is particularly true in our case where we sample neurons that are on the dorsal surface of the striatum, and where it is likely that the activation begins in the more ventral bulk of the striatum. We therefore conclude that the neuropil signal represents bursts of concurrent neuronal discharge of the striatal cholinergic network as a whole. Rather than being considered a signal that needs to be

removed in order to better represent ChI discharge in freely moving mice, it can be considered a mean-field cholinergic signal that is complementary to the signal recorded from individual ChIs. Additionally, our data reveal that this signal propagates spatially – exhibiting wave-like patterns – throughout the striatum. Future work is necessary to determine the behavioral correlates of this propagation.

Discussion

The combination of GECIs and microendoscopic imaging provides an exciting opportunity for studying the collective dynamics of striatal ChIs in freely moving animals. ChIs are autonomously active (Bennett et al., 2000; Goldberg et al., 2009; Surmeier et al., 2005) and have extensive axons and dendritic arbors (Chang et al., 1982; Difiglia, 1987; Kawaguchi, 1992; Wilson et al., 1990). These properties generate a significant neuropil calcium signal. Our investigation of this commonly ignored signal (Pnevmatikakis et al., 2016; Zhou et al., 2018) uncovered a synchronous spatiotemporal wave-like pattern of activation in striatal cholinergic neuropil. Our analysis suggests that bAPs provide the main contribution to the neural activity giving rise to the background signal seen in endoscopy. Finally, we show that the neuropil signal acts as an order parameter representing the striatal ChI network as whole and is, in this sense, similar to LFP (Goldberg, 2004).

Performing endoscopic calcium imaging of pacemaking neurons raises several issues that require careful consideration. First, the proper method of analyzing calcium signals using $\Delta F/F$ as a proxy for changes in calcium concentrations does not allow the detection of baseline spiking activity exhibited by regularly firing pacemakers. We used concurrent calcium imaging and slice electrophysiology to demonstrate that 2PLSM calcium imaging using GCaMP6s only reveals individual spikes in pacemakers if their discharge rate is sufficiently low (~2 spikes/s). This is due to the relatively long decay time constant of GCaMP6s (Chen et al., 2013) that does not allow for the sufficient decay of calcium signals between consecutive spikes. Somatic calcium dynamics may introduce an additional delay (Goldberg et al., 2009), further hindering the detection of single action potentials. In the case of endoscopic imaging, the low sampling rate and low NA associated with miniaturized endoscopes add a major constraint, which makes it difficult to detect individual spikes even

with averaging. Nevertheless, endoscopic calcium imaging has critical advantages over electrophysiological recordings - in particular, the ability to detect spatial patterns in the activity of a molecularly identified neural population.

We exploited this advantage to demonstrate a spatiotemporal structure in the recruitment of striatal cholinergic neuropil. The temporal recruitment is manifested in the slightly slower and earlier rise of the integrated neuropil signal compared to the somatic signals of individual neurons. This is also evident in the negative peak in the CCF between the signals of somata and corresponding annuli. The spatial organization of neuropil recruitment takes the form of a wave-like activity, with a reproducible direction of propagation. The identification of a systematic direction (e.g., between DLS and dorsomedial striatum (DMS)) requires future work, as it is likely to depend on the behavioral context and state of the animal. One possibility is that ChIs in the DLS, believed to be involved in the execution of habitual behaviors, will be activated first when the animal is executing a familiar action, while the ChIs of the DMS may be activated first during exploration and goal-directed behaviors (Ikemoto, 2007; Yin, Knowlton, & Balleine, 2006). It may also be that the robustness of the spatial patterns depends on the level of proficiency of acquired behaviors, with clearer wave-like activity forming during acquisition of an association crucial for the behavior that subsides later on. Finally, it could be that wave-like activity is also present in the neuropil signal of other striatal neurons. These questions will be addressed through future work, partly by studying the relationship of the collective activity of cholinergic somata and neuropil to self-initiated and learned behaviors.

Our results suggest that the background neuropil signal seen in endoscopic *in vivo* calcium imaging arises primarily from the integrated fluorescent signal of bAPs from many ChIs dispersed throughout the striatum (we cannot entirely rule out that subthreshold or synaptically driven calcium influx contribute to the signal, but their contribution is negligible in comparison to suptrathreshold calcium influx). Thus, the cholinergic neuropil signal acts as a mean-field readout of the recurrent activity of the network of striatal ChIs. This is reminiscent of the LFP signal – a once neglected signal that is now extensively studied and believed to represent integrated synaptic activity (Bédard, Kröger, & Destexhe, 2004; Creutzfeldt, Watanabe, & Lux, 1966; Eggermont & Smith, 1995; Goldberg, 2004). We show that fluctuations in neuropil fluorescence are, like fluctuations in the LFP signal (Destexhe,

Contreras, & Steriade, 1999; Eckhorn & Obermueller, 1993), highly correlated in space. In addition, somatic calcium events are preceded by neuropil calcium events. This again resembles the LFP signal, which coincides with increases in instantaneous firing rate (Destexhe et al., 1999; Donoghue et al., 1998; Lass, 1968). Thus, the common practice of subtracting the background signal may be eradicating a signal with physiological significance.

One of the oldest ideas in striatal physiology is that a reciprocal balance between striatal acetylcholine and dopamine levels is necessary for the normal functioning of the striatum (Lehmann & Langer, 1983). Dopamine is a critical neuromodulator mediating both the motivation to engage in a current behavior and the learning of future behaviors (Berke, 2018; Cagniard et al., 2006; Schultz, Apicella, & Ljungberg, 1993; Shiner et al., 2012). Recent studies show that dopamine signals arising from the midbrain and the striatum are dissociated and may be involved in distinct dopaminergic functions (Howe & Dombeck, 2016; Kim et al., 2016; Parker et al., 2016). This requires dopamine recipient circuits to actively switch the way that they interpret dopamine, and striatal ChIs have been proposed as the natural candidates for regulating this switch (Morris, Arkadir, Nevet, Vaadia, & Bergman, 2004; Yamanaka et al., 2018). Thus, the spatial propagation of cholinergic activation might also elicit hot spots and even traveling waves of dopamine concentrations in the striatum. This intriguing idea could be tested in future studies using new optical probes that enable the visualization of local changes in the concentration of dopamine, as well as other neurotransmitters (Patriarchi et al., 2018).

Materials and Methods

Animals

Experimental procedures adhered to and received prior written approval from the Hebrew University Institutional Animal Care and Use Committee. Two-to-nine-months-old choline acetyltransferase-cre dependent (ChAT-IRES-Cre) transgenic mice (stock number 006410; Jackson Laboratories, Bar Harbor, ME, USA) of both sexes were used in the experiments.

Stereotaxic injection of adeno-associated viruses and ChR2

Mice were deeply anesthetized with isoflurane in a non-rebreathing system (2.5% induction, 1–1.5% maintenance) and placed in a stereotaxic frame (model 940, Kopf Instruments, Tujunga, CA, USA). Temperature was maintained at 35°C with a heating pad, artificial tears were applied to prevent corneal drying, and animals were hydrated with a bolus of injectable saline (5 ml/kg) mixed with an analgesic (5 mg/kg carpofen). To calibrate specific injection coordinates, the distance between bregma and lambda bones was measured and stereotaxic placement of the mice was readjusted to achieve maximum accuracy. A small hole was bored into the skull with a micro drill bit and a glass pipette was slowly inserted at the relevant coordinates in aseptic conditions. To minimize backflow, solution was slowly injected and the pipette was left in place for 7 min before slowly retracting it.

A total amount of 400 nl of an adeno-associated virus serotype 9 harboring GCaMP6s construct (AAV9-syn-flex-GCaMP6s; > 2.5 × 10^{13} viral genome/ml; University of Pennsylvania Vector Core, catalog number AV-9-PV2824) was injected into the dorsal striatum under aseptic conditions. The coordinates of the injection were as follows: anteroposterior, +0.5 mm; mediolateral, +2.3 mm; and dorsoventral, −2.8 mm, relative to bregma using a flat skull position (Paxinos, Franklin, Paxinos, G and Franklin, Paxinos, & Franklin, 2004).

As described previously (Aceves Buendia et al., 2017), for thalamic expression of ChR2 a total of 250 nl of an adeno-associated virus serotype 9 harboring ChR2 construct (AAV9-hSyn-ChR2-eGFP; > 2.5 × 10^{13} viral genome/ml; University of Pennsylvania Vector Core, catalog number AV-9-26973P) was injected into the caudal intralaminar nucleus (ILN) of the thalamus to transfect the parafascicular nucleus (PfN) neurons under aseptic conditions. The coordinates of the injection were as follows: anteroposterior, -2.3 mm; mediolateral, +0.65 mm; and dorsoventral, −3.35 mm, relative to bregma using a flat skull position (Ellender, Harwood, Kosillo, Capogna, & Bolam, 2013; Paxinos et al., 2004). Two to three weeks after viral injection mice were used for experiments.

Gradient refractive index (GRIN) lens implantation

One week after the stereotaxic injection, mice were deeply anesthetized with isoflurane in a non-rebreathing system and placed in the stereotaxic frame, as described above (in some cases, a bolus of ketamine (32 mg/kg)-xylasine (3.2 mg/kg) was injected initially to stabilize the preparation for and induction of anesthesia). A hole slightly wider than the 1mm diameter (4 mm long) GRIN lens was drilled into the skull in aseptic conditions. We aspirated cortex with a 27-30 G needle to a depth of approximately 2 mm (just past the corpus callosum) and then fit the lens in snugly and (dental) cemented it into place together with a head bar for restraining the mouse when necessary. One week later we attached a baseplate to guarantee that the endoscope will be properly aligned with the implanted GRIN lens. To ensure light impermeability, the dental cement was mixed with coal powder and painted with black nail polish. Imaging of naïve mice began two weeks later, and was done in a behavior chamber lit with diffuse infrared light as mice were allowed to move freely.

Microendoscopic Imaging

Microendoscopes (*nVista*, Inscopix, Palo Alto, CA, USA) sampled an area of approximately 600 μm by 900 μm (pixel dimension: 1.2 μm) at 10 frames/sec. Imaging and electrophysiological data were analyzed, and curve fitting was performed using custom-made code in MATLAB (MathWorks, Natick, MA, USA). We extracted fluorescence changes over time ($\Delta F/F$) such that $\Delta F/F \stackrel{\text{def}}{=} \frac{F-F_0}{F_0}$. F is the raw fluorescent values recorded; F_0 denotes the minimal averaged fluorescence in 1.5 sec-overlapping 3 sec periods throughout the measurement. Mice with weak transfection or too few somata were discarded. Somata were identified from a long-term temporal maximum projection of the $\Delta F/F$ signal, and small Regions-of-Interest (ROIs) were marked manually within the somatic area. The annulus of each ROI was defined as a ring of pixels with the same area as the ROI, whose inner diameter is the distance of the point on the border of the ROI that is farthest away from the center-of-mass of the ROI plus 5 additional pixels.

Slice preparation

Two to three weeks following AAV injections, mice were deeply anesthetized with intraperitoneal injections of ketamine (200 mg/kg) – xylazine (23.32 mg/kg) and perfused

transcardially with ice-cold modified artificial CSF (ACSF) oxygenated with 95% O_2–5% CO_2 and containing the following (in mM): 2.5 KCl, 26 $NaHCO_3$, 1.25 Na_2HPO_4, 0.5 $CaCl_2$, 10 $MgSO_4$, 10 glucose, 0.4 Ascorbic acid, and 210 sucrose. The brain was removed and blocked in the sagittal plane and sectioned at a thickness of 240 μm in ice-cold modified ACSF. Slices were then submerged in ACSF, bubbled with 95% O_2-5% CO_2, and containing the following (in mM): 2.5 KCl, 126 NaCl, 26 $NaHCO_3$, 1.25 Na2HPO_4, 2 $CaCl_2$, 2 $MgSO_4$, and 10 glucose and stored at room temperature for at least 1 h before recording and/or imaging.

Slice visualization and data collection – wide-field imaging

Slices were transferred to a recording chamber mounted on an Olympus BX51 upright, fixed-stage microscope and perfused with oxygenated ACSF at room temperature. A 20X, 0.5 NA water immersion objective was used to examine the slice using Dodt contrast video microscopy.

Electrophysiology: Electrophysiological recordings were obtained with a Multiclamp 700B amplifier (Molecular Devices, Sunnyvale, CA). Junction potential, which was 7–8 mV, was not corrected. Signals were digitized at 10 kHz. Patch pipette resistance was typically 3–4 MΩ when filled with the recording solution. For calcium imaging experiments in conjunction with current-clamp recordings the pipette contained the following (in mM): 130 K-gluconate, 6 KCl, 8 NaCl, 10 HEPES, $2Mg_{1.5}ATP$, pH 7.3 with KOH (280–290 mOsm/kg).

One-photon wide-field calcium imaging: Optical measurements were made using 470 nm LED illumination (Mightex, Toronto, ON, Canada) and a cooled EM-CCD (Evolve 512 Delta, Photometrics, Tucson, AZ, USA). Frames were 512×512 pixels, pixel size was 0.4 μm with no binning and frame rate was 5-10 Hz. Regions of interest were marked manually offline and fluorescent traces were extracted.

Optical and electrophysiological data were obtained using the custom-made shareware package WinFluor (John Dempster, Strathclyde University, Glasgow, Scotland, UK), which automates and synchronizes the imaging signals and electrophysiological protocols. $\Delta F/F$ (for all acute slice experiments) was calculated as defined above with F_0 defined as the minimal value attained during the trace.

Slice visualization and data collection – 2PLSM

The slices were transferred to the recording chamber of Femto2D-Galvo scanner multiphoton system (Femtonics Ltd., Budapest, Hungary) and perfused with oxygenated

ACSF at room temperature. A 16X, 0.8 NA water immersion objective was used to examine the slice using oblique illumination.

Electrophysiology: Electrophysiological recordings were obtained with a Multiclamp 700B amplifier (Molecular Devices, Sunnyvale, CA). Junction potential, which was 7–8 mV, was not corrected. Signals were digitized at 40 kHz. Patch pipette resistance and solution were as described for one-photon experiments.

2PLSM calcium imaging: The 2PLSM excitation source was a Chameleon Vision 2 tunable pulsed laser system (680–1,080 nm; Coherent Laser Group, Santa Clara, CA). Optical imaging of GCaMP6s signals was performed by using a 920-nm excitation beam. The GCaMP6s emission was detected and collected with gated GaAsP photomultiplier tubes (PMTs) for high sensitivity detection of fluorescence photons as part of the Femto2D-Galvo scanner. The laser light transmitted through the sample was collected by the condenser lens and sent to another PMT to provide a bright-field transmission image in registration with the fluorescent images. Line scans were marked through the somata and visible dendrites and 20–250 Hz scans were performed, using ~0.2-μm pixels and an 8-12 μs dwell time. ROIs were marked manually offline based on the online marked line scans and fluorescent traces were extracted.

Optical and electrophysiological data were obtained using the software package MES (Femtonics), which also integrates the control of all hardware units in the microscope. The software automates and synchronizes the imaging signals and electrophysiological protocols. Data was extracted from the MES package to personal computers using custom-made code in MATLAB.

Somatic current injection

To generate subthreshold depolarizations, we injected 8-12 pA for 800 ms such that the voltage almost reached the threshold of activation. A 5 ms long, 500 pA pulse was used to generate an action potential. To calculate the calcium response to the stimulations we subtracted the baseline fluorescent level 50 ms prior to the stimulations and calculated the integrated $\Delta F/F$ over a duration 800 ms from the start time of the stimulation both for sub- and supra-threshold depolarizations.

Spike triggered averaging (STA) and model

To generate the STA, we averaged the $\Delta F/F$ signal around spike times. To fit the dependence of the amplitude of the STA on firing rate (Fig. 5F) we used a phenomenological model. Let τ be the decay time constant of GCaMP. Assume a periodic neuron with an inter spike interval of duration T, such that $f=1/T$ is the firing frequency. The decay of the GCaMP fluorescence can be modeled as $e^{-\frac{1}{f\tau}}$. If F_0 is the baseline fluorescence level and ΔF is the amplitude of the fluorescence calcium trace visible over the baseline fluorescence, then the equation describing the decay of the GCaMP from its maximum value to baseline value is as follows:

$$(F_0 + \Delta F) \cdot e^{-\frac{1}{f\tau}} = F_0$$
$$\Leftrightarrow \frac{\Delta F}{F_0} = e^{\frac{1}{f\tau}} - 1$$

Optogenetic stimulation

Blue light LED of the Femto2D-Galvo scanner multiphoton system (473 nm, Femtonics) was used for full-field illumination. Light pulse trains consisted of 5 pulses at 10 Hz, each pulse lasting 1ms. Fast gated GaAsP PMTs were used perform imaging in 2PLSM without saturating the PMTs due to the LED light. The PMTs were disabled 5 ms prior to LED flash and re-enabled 5 ms after the end of the light flash. To calculate the calcium response in response to the optogenetic stimulation, we subtracted the baseline fluorescence prior to the stimulations (50 ms prior to stimulation time), and compared the integrated dendritic calcium signal during a 200 ms window beginning 500 ms after evoking sub-threshold EPSPs, to the dendritic calcium signal generated by spontaneously occurring bAPs for that same time window in the same neurons.

Immunohistochemistry

Tissue preparation and the staining protocols were performed as described previously (Chiu et al., 2014). Briefly, animals were deeply anesthetized and perfused transcardially with 0.1 M phosphate buffer (PB) followed by ice-cold 4% paraformaldehyde (PFA). Coronal sections of the striatum were cut at 30 μm on a cryostat microtome (Leica CM1950) in antifreeze buffer (1:1:3 volume ratio of ethyl glycerol, glycerol, and 0.1 M PB) and stored at −20°C before further analysis. The sections were preincubated in 5% normal

horse serum and 0.3% Triton X-100 in 0.1 M PB for 40 min after washing steps, and incubated overnight at 4°C with the primary antibodies [goat anti-choline acetyltransferase (ChAT), 1:100 (Millipore; RRID: AB_262156)]. On the second day, sections were incubated with fluorophore-conjugated species-specific secondary antibodies [donkey anti-goat, 1:1000 (Abcam)] for 2 h at room temperature. Brain sections were rinsed in PBS and directly cover-slipped by fluorescent mounting medium (Vectashield, Vector Laboratories). Multilabeling fluorescent immunostainings of juxtacellularly filled neurons were analyzed using a laser-scanning microscope (LSM 510 Meta, Zeiss) using 20X/0.3 NA interference contrast lens (20X zoom).

Data and statistical analysis

Calculating the velocity vector of the propagation of the neuropil signal: We generated a latency map $\tau(x_i,y_j)$ of the imaged region (which is an L_x by L_y rectangle) , in which the entry in each pixel (x_i,y_j) is the latency at which the $\Delta F/F$ signal (averaged around all of the peak events of the spatially averaged $\Delta F/F$ signal) peaks relative to the timing of the peak of the spatially averaged $\Delta F/F$ signal. We calculated the components of the velocity vector of the propagation as

$$v_x = \frac{{L_x}^2/12}{\int_{-L_x/2}^{L_x/2} \frac{dx}{L_x} x \int_{-L_y/2}^{L_y/2} \frac{dy}{L_y} \tau(x,y)}$$

$$v_y = \frac{{L_y}^2/12}{\int_{-L_y/2}^{L_y/2} \frac{dy}{L_y} y \int_{-L_x/2}^{L_x/2} \frac{dx}{L_x} \tau(x,y)}$$

which is the solution of a least-square fit of the model $x/v_x + y/v_y + const.$ to the function $\tau(x,y)$ (after setting all the pixels in the image that are outside the lens to zero). Peak events in the spatial average were detected with a peak-finding algorithm (MATLAB) with the condition that the peak amplitude be larger than 35% $\Delta F/F$.

The nonparametric two-tailed Wilcoxon signed-rank test (SRT) was used for matched samples. Null hypotheses were rejected if the *P*-value was below 0.05.

Acknowledgments

We would like to thank Dr. Yaniv Ziv for his expert guidance and advice. Eng. Anatoly Shapochnikov offered excellent technical support. This work was funded by a European Research Council (ERC) Consolidator Grant (no. 646886 – SynChI) and two grants from the Israel Science Foundation (ISF, nos. 154/14 and 155/14) to J.A.G.

Author Contribution

R.R. Y.A. and L.T. conceptualized, designed and conducted the experiments, analyzed the data, and wrote the paper. W-H.C. conducted the histology. J.J.A.B and G.J.M. helped with initial stages of setting up the endoscopy experiments and instrumenting the mice. G.A.J. conceptualized and supervised the experiments, analyzed data and wrote the paper. J.A.G. conceptualized, designed and supervised the experiments, wrote the paper, secured funding and is responsible for the content of the manuscript.

Declaration of Interests

That authors declare no competing interests.

References

Aceves Buendia, J. de J., Tiroshi, L., Chiu, W. H., & Goldberg, J. A. (2017, October 6). Selective remodeling of glutamatergic transmission to striatal cholinergic interneurons after dopamine depletion. *European Journal of Neuroscience*. Wiley/Blackwell (10.1111). https://doi.org/10.1111/ejn.13715

Anderson, M. E. (1978). Discharge patterns of basal ganglia neurons during active maintenance of postural stability and adjustment to chair tilt. *Brain Research*, *143*(2), 325–338. https://doi.org/10.1016/0006-8993(78)90572-3

Aosaki, T., Graybiel, A. M., & Kimura, M. (1994). Effect of the nigrostriatal dopamine system on acquired neural responses in the striatum of behaving monkeys. *Science*, *265*(July), 412–415. https://doi.org/10.1126/science.8023166

Apicella, P., Legallet, E., & Trouche, E. (1997). Responses of tonically discharging neurons in the monkey striatum to primary rewards delivered during different behavioral states. *Experimental Brain Research*, *116*(3), 456–466. https://doi.org/10.1007/PL00005773

Bédard, C., Kröger, H., & Destexhe, A. (2004). Modeling Extracellular Field Potentials and the Frequency-Filtering Properties of Extracellular Space. *Biophysical Journal*, *86*(3), 1829–1842. https://doi.org/10.1016/S0006-3495(04)74250-2

Bennett, B. D., Callaway, J. C., & Wilson, C. J. (2000). Intrinsic membrane properties underlying spontaneous tonic firing in neostriatal cholinergic interneurons. *The Journal of Neuroscience*, *20*(22), 8493–8503. https://doi.org/20/22/8493 [pii]

Bennett, B. D., & Wilson, C. J. (1999). Spontaneous activity of neostriatal cholinergic interneurons in

vitro. *The Journal of Neuroscience*, *19*(13), 5586–96. https://doi.org/papers://464828DA-1475-4871-9F92-73166AE8F283/Paper/p1174

Berke, J. D. (2018). What does dopamine mean? *Nature Neuroscience*, *21*(6), 787–793. https://doi.org/10.1038/s41593-018-0152-y

Bullock, T. H. (1997). Signals and signs in the nervous system: the dynamic anatomy of electrical activity is probably information-rich. *Proceedings of the National Academy of Sciences of the United States of America*, *94*(1), 1–6. https://doi.org/10.1073/PNAS.94.1.1

Cachope, R., Mateo, Y., Mathur, B. N., Irving, J., Wang, H. L., Morales, M., … Cheer, J. F. (2012). Selective activation of cholinergic interneurons enhances accumbal phasic dopamine release: Setting the tone for reward processing. *Cell Reports*, *2*(1), 33–41. https://doi.org/10.1016/j.celrep.2012.05.011

Cagniard, B., Beeler, J. A., Britt, J. P., McGehee, D. S., Marinelli, M., & Zhuang, X. (2006). Dopamine scales performance in the absence of new learning. *Neuron*, *51*(5), 541–547. https://doi.org/10.1016/J.NEURON.2006.07.026

Calabresi, P., Centonze, D., Gubellini, P., Pisani, A., & Bernardi, G. (2000). Acetylcholine-mediated modulation of striatal function. *Trends in Neurosciences*. https://doi.org/10.1016/S0166-2236(99)01501-5

Chang, H. T., Wilson, C. J., & Kitai, S. T. (1982). A Golgi study of rat neostriatal neurons: Light microscopic analysis. *The Journal of Comparative Neurology*, *208*(2), 107–126. https://doi.org/10.1002/cne.902080202

Chen, T.-W., Wardill, T. J., Sun, Y., Pulver, S. R., Renninger, S. L., Baohan, A., … Kim, D. S. (2013). Ultrasensitive fluorescent proteins for imaging neuronal activity. *Nature*, *499*(7458), 295–300. https://doi.org/10.1038/nature12354

Chiu, W. H., Carlsson, T., Depboylu, C., Höglinger, G. U., Oertel, W. H., & Ries, V. (2014). Selegiline normalizes, while l-DOPA sustains the increased number of dopamine neurons in the olfactory bulb in a 6-OHDA mouse model of Parkinson's disease. *Neuropharmacology*, *79*, 212–221. https://doi.org/10.1016/j.neuropharm.2013.11.014

Chuhma, N., Mingote, S., Moore, H., & Rayport, S. (2014). Dopamine neurons control striatal cholinergic neurons via regionally heterogeneous dopamine and glutamate signaling. *Neuron*, *81*(4), 901–912. https://doi.org/10.1016/j.neuron.2013.12.027

Contant, C., Umbriaco, D., Garcia, S., Watkins, K. C., & Descarries, L. (1996). Ultrastructural characterization of the acetylcholine innervation in adult rat neostriatum. *Neuroscience*, *71*(4), 937–947. https://doi.org/10.1016/0306-4522(95)00507-2

Creutzfeldt, O. D., Watanabe, S., & Lux, H. D. (1966). Relations between EEG phenomena and potentials of single cortical cells. II. Spontaneous and convulsoid activity. *Electroencephalography and Clinical Neurophysiology*, *20*(1), 19–37. https://doi.org/10.1016/0013-4694(66)90137-4

Dautan, D., Huerta-Ocampo, I., Witten, I. B., Deisseroth, K., Bolam, J. P., Gerdjikov, T., & Mena-Segovia, J. (2014). A Major External Source of Cholinergic Innervation of the Striatum and Nucleus Accumbens Originates in the Brainstem. *Journal of Neuroscience*, *34*(13), 4509–4518. https://doi.org/10.1523/JNEUROSCI.5071-13.2014

Destexhe, A., Contreras, D., & Steriade, M. (1999). Spatiotemporal analysis of local field potentials and unit discharges in cat cerebral cortex during natural wake and sleep states. *The Journal of Neuroscience*, *19*(11), 4595–608. https://doi.org/10.1523/JNEUROSCI.19-11-04595.1999

Difiglia, M. (1987). Synaptic organization of cholinergic neurons in the monkey neostriatum. *The Journal of Comparative Neurology*, *255*(2), 245–258. https://doi.org/10.1002/cne.902550208

Ding, J. B., Guzman, J. N., Peterson, J. D., Goldberg, J. A., & Surmeier, D. J. (2010). Thalamic gating of corticostriatal signaling by cholinergic interneurons. *Neuron*, *67*(2), 294–307. https://doi.org/10.1016/J.NEURON.2010.06.017

Donoghue, J. P., Sanes, J. N., Hatsopoulos, N. G., & Gaál, G. (1998). Neural discharge and local field

potential oscillations in primate motor cortex during voluntary movements. *Journal of Neurophysiology*, *79*(1), 159–173. https://doi.org/10.1152/jn.1998.79.1.159

Eckhorn, R., & Obermueller, A. (1993). Single neurons are differently involved in stimulus-specific oscillations in cat visual cortex. *Experimental Brain Research*, *95*(1), 177–182. https://doi.org/10.1007/BF00229667

Eggermont, J. J., & Smith, G. M. (1995). Synchrony between single-unit activity and local field potentials in relation to periodicity coding in primary auditory cortex. *Journal of Neurophysiology*, *73*(1), 227–45. https://doi.org/10.1152/jn.1995.73.1.227

Ellender, T. J., Harwood, J., Kosillo, P., Capogna, M., & Bolam, J. P. (2013). Heterogeneous properties of central lateral and parafascicular thalamic synapses in the striatum. *The Journal of Physiology*, *591*(1), 257–272. https://doi.org/10.1113/jphysiol.2012.245233

English, D. F., Ibanez-Sandoval, O., Stark, E., Tecuapetla, F., Buzsáki, G., Deisseroth, K., … Koos, T. (2011). GABAergic circuits mediate the reinforcement-related signals of striatal cholinergic interneurons. *Nature Neuroscience*, *15*(1), 123–130. https://doi.org/10.1038/nn.2984

Ghosh, K. K., Burns, L. D., Cocker, E. D., Nimmerjahn, A., Ziv, Y., Gamal, A. El, & Schnitzer, M. J. (2011). Miniaturized integration of a fluorescence microscope. *Nature Methods*, *8*(10), 871–878. https://doi.org/10.1038/nmeth.1694

Goldberg, J. A. (2004). Spike Synchronization in the Cortex-Basal Ganglia Networks of Parkinsonian Primates Reflects Global Dynamics of the Local Field Potentials. *Journal of Neuroscience*, *24*(26), 6003–6010. https://doi.org/10.1523/JNEUROSCI.4848-03.2004

Goldberg, J. A., Boraud, T., Maraton, S., Haber, S. N., Vaadia, E., & Bergman, H. (2002). Enhanced synchrony among primary motor cortex neurons in the 1-methyl-4-phenyl-1,2,3,6-tetrahydropyridine primate model of Parkinson's disease. *The Journal of Neuroscience : The Official Journal of the Society for Neuroscience*, *22*(11), 4639–4653. https://doi.org/20026424

Goldberg, J. A., Ding, J. B., & Surmeier, D. J. (2012). Muscarinic modulation of striatal function and circuitry. *Handbook of Experimental Pharmacology*. Springer Berlin Heidelberg. https://doi.org/10.1007/978-3-642-23274-9_10

Goldberg, J. A., Teagarden, M. A., Foehring, R. C., & Wilson, C. J. (2009). Nonequilibrium Calcium Dynamics Regulate the Autonomous Firing Pattern of Rat Striatal Cholinergic Interneurons. *Journal of Neuroscience*, *29*(26), 8396–8407. https://doi.org/10.1523/JNEUROSCI.5582-08.2009

Goldberg, J. A., & Wilson, C. J. (2010). The cholinergic interneurons of the striatum: intrinsic properties underlie multiple discharge patterns. In H. Steiner & K. Y. Tseng (Eds.), *Handbook of Basal Ganglia Structure and Function* (Vol. 20, pp. 133–149). https://doi.org/10.1016/B978-0-12-374767-9.00007-X

Graybiel, A., Aosaki, T., Flaherty, A., & Kimura, M. (1994). The basal ganglia and adaptive motor control. *Science*, *265*(5180), 1826–1831. https://doi.org/10.1126/science.8091209

Grynkiewicz, G., Poenie, M., & Tsien, R. Y. (1985). A new generation of Ca2+ indicators with greatly improved fluorescence properties. *Journal of Biological Chemistry*, *260*(6), 3440–3450. https://doi.org/3838314

Howe, M. W., & Dombeck, D. A. (2016). Rapid signalling in distinct dopaminergic axons during locomotion and reward Locomotion related dopamine signalling. *Nature*. https://doi.org/10.1038/nature18942

Ikemoto, S. (2007). Dopamine reward circuitry: Two projection systems from the ventral midbrain to the nucleus accumbens–olfactory tubercle complex. *Brain Research Reviews*, *56*(1), 27–78. https://doi.org/10.1016/J.BRAINRESREV.2007.05.004

Karnani, M. M., Jackson, J., Ayzenshtat, I., Tucciarone, J., Manoocheri, K., Snider, W. G., & Yuste, R. (2016). Cooperative subnetworks of molecularly similar interneurons in mouse neocortex. *Neuron*, *90*(1), 86–100. https://doi.org/10.1016/J.NEURON.2016.02.037

Kawaguchi, Y. (1992). Large aspiny cells in the matrix of the rat neostriatum in vitro: physiological

identification, relation to the compartments and excitatory postsynaptic currents. *Journal of Neurophysiology*, *67*(6), 1669–82. https://doi.org/10.1152/jn.1992.67.6.1669

Kim, C. K., Yang, S. J., Pichamoorthy, N., Young, N. P., Kauvar, I., Jennings, J. H., … Deisseroth, K. (2016). Simultaneous fast measurement of circuit dynamics at multiple sites across the mammalian brain. *Nature Methods*, *13*(4), 325–328. https://doi.org/10.1038/nmeth.3770

Kimura, M., Rajkowski, J., & Evarts, E. (1984). Tonically discharging putamen neurons exhibit set-dependent responses. *Neurobiology*, *81*, 4998–5001. https://doi.org/10.1073/pnas.81.15.4998

Klaus, A., Martins, G. J., Paixao, V. B., Zhou, P., Paninski, L., & Costa, R. M. (2017). The spatiotemporal organization of the striatum encodes action space. *Neuron*, *95*(5), 1171–1180.e7. https://doi.org/10.1016/J.NEURON.2017.08.015

Klaus, A., & Plenz, D. (2016). A low-correlation resting state of the striatum during cortical avalanches and its role in movement suppression. *PLOS Biology*, *14*(12), e1002582. https://doi.org/10.1371/journal.pbio.1002582

Lapper, S. R., & Bolam, J. P. (1992). Input from the frontal cortex and the parafascicular nucleus to cholinergic interneurons in the dorsal striatum of the rat. *Neuroscience*, *51*(3), 533–545.

Lass, Y. (1968). A quantitative approach to the correlation of slow wave and unit electrical activity in the cerebral cortex of the cat. *Electroencephalography and Clinical Neurophysiology*, *25*(5), 503–506. https://doi.org/10.1016/0013-4694(68)90162-4

Lehmann, J., & Langer, S. Z. (1983). The striatal cholinergic interneuron: Synaptic target of dopaminergic terminals? *Neuroscience*, *10*(4), 1105–1120. https://doi.org/10.1016/0306-4522(83)90102-1

Lin, M. Z., & Schnitzer, M. J. (2016). Genetically encoded indicators of neuronal activity. *Nature Neuroscience*, *19*(9), 1142–1153. https://doi.org/10.1038/nn.4359

Malvache, A., Reichinnek, S., Villette, V., Haimerl, C., & Cossart, R. (2016). Awake hippocampal reactivations project onto orthogonal neuronal assemblies. *Science*, *353*(6305), 1280–3. https://doi.org/10.1126/science.aaf3319

Mank, M., & Griesbeck, O. (2008). Genetically encoded calcium indicators. *Chemical Reviews*. https://doi.org/10.1021/cr078213v

Mesulam, M.-M., Mash, D., Hersh, L., Bothwell, M., & Geula, C. (1992). Cholinergic innervation of the human striatum, globus pallidus, subthalamic nucleus, substantia nigra, and red nucleus. *The Journal of Comparative Neurology*, *323*(2), 252–268. https://doi.org/10.1002/cne.903230209

Morris, G., Arkadir, D., Nevet, A., Vaadia, E., & Bergman, H. (2004). Coincident but distinct messages of midbrain dopamine and striatal tonically active neurons. *Neuron*. https://doi.org/10.1016/j.neuron.2004.06.012

Nakai, J., Ohkura, M., & Imoto, K. (2001). A high signal-to-noise Ca2+ probe composed of a single green fluorescent protein. *Nature Biotechnology*, *19*(2), 137–41. https://doi.org/10.1038/84397

Nelson, A. B., Hammack, N., Yang, C. F., Shah, N. M., Seal, R. P., & Kreitzer, A. C. (2014). Striatal cholinergic interneurons drive GABA release from dopamine terminals. *Neuron*, *82*(1), 63–70. https://doi.org/10.1016/j.neuron.2014.01.023

Pakhotin, P., & Bracci, E. (2007). Cholinergic interneurons control the excitatory input to the striatum. *Journal of Neuroscience*, *27*(2), 391–400. https://doi.org/10.1523/JNEUROSCI.3709-06.2007

Parker, N. F., Cameron, C. M., Taliaferro, J. P., Lee, J., Choi, J. Y., Davidson, T. J., … Witten, I. B. (2016). Reward and choice encoding in terminals of midbrain dopamine neurons depends on striatal target. *Nature Neuroscience*, *19*(6), 845–854. https://doi.org/10.1038/nn.4287

Patriarchi, T., Cho, J. R., Merten, K., Howe, M. W., Marley, A., Xiong, W.-H., … Tian, L. (2018). Ultrafast neuronal imaging of dopamine dynamics with designed genetically encoded sensors. *Science*, *360*(6396), eaat4422. https://doi.org/10.1126/science.aat4422

Paxinos, G., Franklin, K. B. J., Paxinos, G and Franklin, K. B. J., Paxinos, G., & Franklin, K. B. J. (2004). *Mouse Brain in Stereotaxic Coordinates*. *Academic Press* (Vol. 2nd). https://doi.org/10.1016/S0306-4530(03)00088-X

Pisani, A., Bernardi, G., Ding, J., & Surmeier, D. J. (2007). Re-emergence of striatal cholinergic interneurons in movement disorders. *Trends in Neurosciences*. https://doi.org/10.1016/j.tins.2007.07.008

Pnevmatikakis, E. A., Soudry, D., Gao, Y., Machado, T. A., Merel, J., Pfau, D., … Paninski, L. (2016). Simultaneous denoising, deconvolution, and demixing of calcium imaging data. *Neuron*, *89*(2), 285–299. https://doi.org/10.1016/J.NEURON.2015.11.037

Ravel, S., Legallet, E., & Apicella, P. (2003). Responses of tonically active neurons in the monkey striatum discriminate between motivationally opposing stimuli. *The Journal of Neuroscience*, *23*(24), 8489–97. https://doi.org/10.1523/JNEUROSCI.23-24-08489.2003

Raz, A., Feingold, A., Zelanskaya, V., Vaadia, E., & Bergman, H. (1996). Neuronal synchronization of tonically active neurons in the striatum of normal and parkinsonian primates. *Journal of Neurophysiology*, *76*(3).

Redish, A. D., Battaglia, F. P., Chawla, M. K., Ekstrom, A. D., Gerrard, J. L., Lipa, P., … Barnes, C. A. (2001). Independence of firing correlates of anatomically proximate hippocampal pyramidal cells. *The Journal of Neuroscience : The Official Journal of the Society for Neuroscience*, *21*(5), RC134. https://doi.org/20015093 [pii]

Rubin, A., Geva, N., Sheintuch, L., & Ziv, Y. (2015). Hippocampal ensemble dynamics timestamp events in long-term memory. *ELife*, *4*(December). https://doi.org/10.7554/eLife.12247

Schultz, W., Apicella, P., & Ljungberg, T. (1993). Responses of monkey dopamine neurons to reward and conditioned stimuli during successive steps of learning a delayed response task. *The Journal of Neuroscience*, *13*(3), 900–13. https://doi.org/10.1523/JNEUROSCI.13-03-00900.1993

Shiner, T., Seymour, B., Wunderlich, K., Hill, C., Bhatia, K. P., Dayan, P., & Dolan, R. J. (2012). Dopamine and performance in a reinforcement learning task: evidence from Parkinson's disease. *Brain*, *135*(6), 1871–1883. https://doi.org/10.1093/brain/aws083

Stamatakis, A. M., Schachter, M. J., Gulati, S., Zitelli, K. T., Malanowski, S., Tajik, A., … Otte, S. L. (2018). Simultaneous optogenetics and cellular resolution calcium imaging during active behavior using a miniaturized microscope. *Frontiers in Neuroscience*, *12*, 496. https://doi.org/10.3389/fnins.2018.00496

Surmeier, D. J., Mercer, J. N., & Chan, C. S. (2005). Autonomous pacemakers in the basal ganglia: Who needs excitatory synapses anyway? *Current Opinion in Neurobiology*, *15*(3 SPEC. ISS.), 312–318. https://doi.org/10.1016/j.conb.2005.05.007

Tanimura, A., Lim, S. A. O., Aceves Buendia, J. de J., Goldberg, J. A., & Surmeier, D. J. (2016). Cholinergic interneurons amplify corticostriatal synaptic responses in the Q175 model of Huntington's disease. *Frontiers in Systems Neuroscience*, *10*, 102. https://doi.org/10.3389/fnsys.2016.00102

Teagarden, M., Atherton, J. F., Bevan, M. D., & Wilson, C. J. (2008). Accumulation of cytoplasmic calcium, but not apamin-sensitive afterhyperpolarization current, during high frequency firing in rat subthalamic nucleus cells. *The Journal of Physiology*, *586*(3), 817–833. https://doi.org/10.1113/jphysiol.2007.141929

Threlfell, S., Lalic, T., Platt, N. J., Jennings, K. A., Deisseroth, K., & Cragg, S. J. (2012). Striatal dopamine release is triggered by synchronized activity in cholinergic interneurons. *Neuron*, *75*(1), 58–64. https://doi.org/10.1016/j.neuron.2012.04.038

Wilson, C. J. (2004). Basal ganglia. In *The synaptic organization of the brain* (5th ed., pp. 361–414). Shepherd GM (Oxford Univ Press, Oxford).

Wilson, C. J., Chang, H. T., & Kitai, S. T. (1990). Firing patterns and synaptic potentials of identified giant aspiny interneurons in the rat neostriatum. *Journal of Neuroscience*, *10*(0270–6474

(Print)), 508–519. https://doi.org/10.3389/fnsys.2011.00083

Yamanaka, K., Hori, Y., Minamimoto, T., Yamada, H., Matsumoto, N., Enomoto, K., … Kimura, M. (2018). Roles of centromedian parafascicular nuclei of thalamus and cholinergic interneurons in the dorsal striatum in associative learning of environmental events. *Journal of Neural Transmission*, *125*(3), 501–513. https://doi.org/10.1007/s00702-017-1713-z

Yin, H. H., Knowlton, B. J., & Balleine, B. W. (2006). Inactivation of dorsolateral striatum enhances sensitivity to changes in the action–outcome contingency in instrumental conditioning. *Behavioural Brain Research*, *166*(2), 189–196. https://doi.org/10.1016/J.BBR.2005.07.012

Zhou, P., Resendez, S. L., Rodriguez-Romaguera, J., Jimenez, J. C., Neufeld, S. Q., Stuber, G. D., … Paninski, L. (2018). Efficient and accurate extraction of in vivo calcium signals from microendoscopic video data. *ELife*, *7*. https://doi.org/10.7554/eLife.28728

Supplementary Material

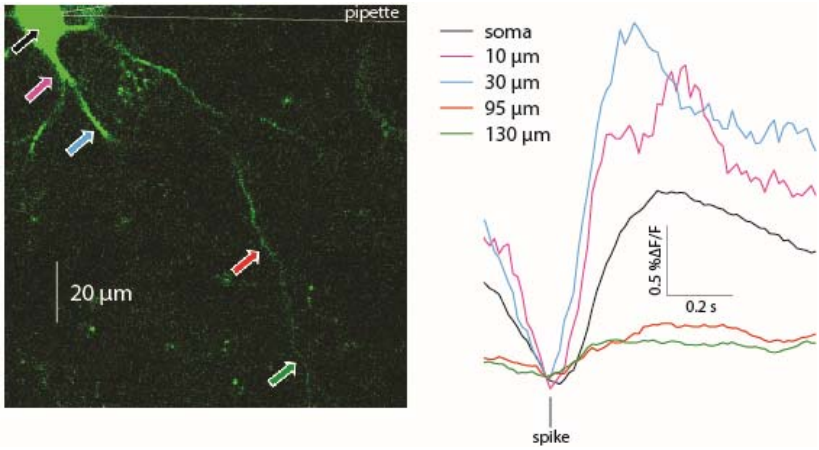

Supplementary Figure 1. Spike triggered averages of calcium transients elicited by bAPs (and imaged with 2PLSM) at various distances from the soma.

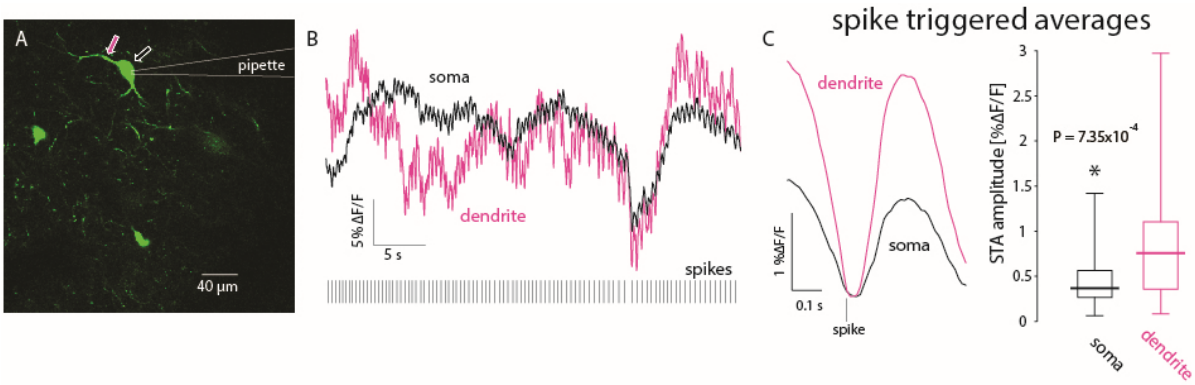

Supplementary Figure 2. Dendritic calcium transients are larger than somatic ones. A. 2PLSM imaging of somatic and dendritic calcium *(ΔF/F)* signals in conjunction with electrophysiological recording from GCaMP6s-expressing ChI. B. Calcium (*ΔF/F*) responses in soma (black) and proximal dendrite (pink) during spontaneous discharge (bottom). C. STA of proximal dendritic (pink) calcium signals is larger than the somatic (black) signal. Right: paired comparison of the amplitude of somatic and dendritic STAs.

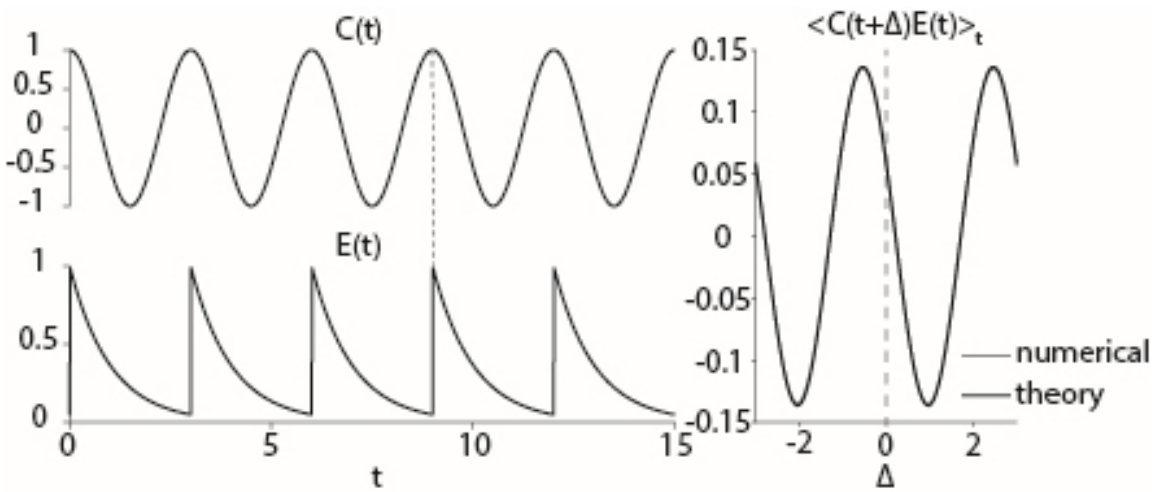

Supplementary Figure 3. Cross-covariance function (CCF) between a slow-rising function and a fast-rising function that both peak at the same times peaks at a negative delay. Consider two periodic functions with the same period T: a sinusoidal $C(t) = cos(2\pi t/T)$, and an exponential saw-tooth function ($E(t) = e^{-\frac{t \bmod T}{\tau}}$) that peak at the same points. Their CCF is given

$$CCF(\Delta) = \langle C(t+\Delta)E(t)\rangle_t = \int_0^T \frac{dt}{T} e^{-\frac{t}{\tau}} cos(2\pi[t+\Delta]/T) = \frac{\tau}{T}\frac{1-e^{-T/\tau}}{\sqrt{1+(2\pi\tau/T)^2}} cos(2\pi[\Delta - D]/T)$$

where $D = -\frac{T}{2\pi} arctan(2\pi\tau/T)$ is the location of the peak of the CCF (in the figure $T = 3$, $\tau = 1$).